



Title	Extending nudged elastic band method to reaction pathways involving multiple spin states
Author(s)	Zhao, Liming; Watanabe, K-jiro; Nakatani, Naoki; Nakayama, Akira; Xu, Xin; Hasegawa, Jun-ya
Citation	Journal of chemical physics, 153(13), 134114 <a href="https://doi.org/10.1063/5.0021923">https://doi.org/10.1063/5.0021923</a>
Issue Date	2020-10-07
Doc URL	<a href="http://hdl.handle.net/2115/82902">http://hdl.handle.net/2115/82902</a>
Rights	This article may be downloaded for personal use only. Any other use requires prior permission of the author and AIP Publishing. This article appeared in Liming Zhao, K-jiro Watanabe, Naoki Nakatani, Akira Nakayama, Xin Xu, and Jun-ya Hasegawa. Extending nudged elastic band method to reaction pathways involving multiple spin states. The Journal of Chemical Physics, 153(13), 134114 (2020) and may be found at <a href="https://doi.org/10.1063/5.0021923">https://doi.org/10.1063/5.0021923</a>
Type	article
File Information	5.0021923.pdf



[Instructions for use](#)

# Extending nudged elastic band method to reaction pathways involving multiple spin states

Cite as: J. Chem. Phys. **153**, 134114 (2020); <https://doi.org/10.1063/5.0021923>

Submitted: 15 July 2020 . Accepted: 15 September 2020 . Published Online: 06 October 2020

Liming Zhao, K-jiro Watanabe,  Naoki Nakatani,  Akira Nakayama,  Xin Xu, and  Jun-ya Hasegawa



View Online



Export Citation



CrossMark

## ARTICLES YOU MAY BE INTERESTED IN

[Rare events and first passage time statistics from the energy landscape](#)

The Journal of Chemical Physics **153**, 134115 (2020); <https://doi.org/10.1063/5.0016244>

[Analytic energy gradients for the self-consistent direct random phase approximation](#)

The Journal of Chemical Physics **153**, 134113 (2020); <https://doi.org/10.1063/5.0021809>

[Enhanced Jarzynski free energy calculations using weighted ensemble](#)

The Journal of Chemical Physics **153**, 134116 (2020); <https://doi.org/10.1063/5.0020600>



New

SHFQA  
Quantum Analyzer  
8.5GHz

Zurich  
Instruments

## Your Qubits. Measured.

Meet the next generation of quantum analyzers

- Readout for up to 64 qubits
- Operation at up to 8.5 GHz, mixer-calibration-free
- Signal optimization with minimal latency

Find out more



# Extending nudged elastic band method to reaction pathways involving multiple spin states

Cite as: J. Chem. Phys. 153, 134114 (2020); doi: 10.1063/5.0021923

Submitted: 15 July 2020 • Accepted: 15 September 2020 •

Published Online: 6 October 2020



View Online



Export Citation



CrossMark

Liming Zhao,<sup>1</sup> K-jiro Watanabe,<sup>1</sup> Naoki Nakatani,<sup>2</sup>  Akira Nakayama,<sup>3</sup>  Xin Xu,<sup>4</sup>  and Jun-ya Hasegawa<sup>1,a)</sup> 

## AFFILIATIONS

<sup>1</sup>Institute for Catalysis, Hokkaido University, N21 W10 Kita-ku, Sapporo 001-0021, Hokkaido, Japan

<sup>2</sup>Graduate School of Science and Engineering, Tokyo Metropolitan University, Minami-Osawa 1-1, Tokyo 192-0397, Japan

<sup>3</sup>Department of Chemical System Engineering, The University of Tokyo, Tokyo 113-8656, Japan

<sup>4</sup>Department of Chemistry, Fudan University, Shanghai 200433, China

<sup>a)</sup> Author to whom correspondence should be addressed: [hasegawa@cat.hokudai.ac.jp](mailto:hasegawa@cat.hokudai.ac.jp)

## ABSTRACT

There are diverse reactions including spin-state crossing, especially the reactions catalyzed by transition metal compounds. To figure out the mechanisms of such reactions, the discussion of minimum energy intersystem crossing (MEISC) points cannot be avoided. These points may be the bottleneck of the reaction or inversely accelerate the reactions by providing a better pathway. It is of great importance to reveal their role in the reactions by computationally locating the position of the MEISC points together with the reaction pathway. However, providing a proper initial guess for the structure of the MEISC point is not as easy as that of the transition state. In this work, we extended the nudged elastic band (NEB) method for multiple spin systems, which is named the multiple spin-state NEB method, and it is successfully applied to find the MEISC points while optimizing the reaction pathway. For more precisely locating the MEISC point, a revised approach was adopted. Meanwhile, our examples also suggest that special attention should be paid to the criterion to define an image optimized as the MEISC point.

Published under license by AIP Publishing. <https://doi.org/10.1063/5.0021923>

## I. INTRODUCTION

One of the most important tasks in the study of chemical reactions is to figure out the mechanism. Finding out the reaction pathway, also known as the minimum energy pathway (MEP), and the corresponding transition states (TSs) is the key to unlock this problem. For nonadiabatic processes such as photophysical and photochemical reactions, the conical intersection point is nonnegligible to explain the mechanism.<sup>1–6</sup> In particular, the molecular structure at the minimal energy conical intersection point is of great importance because it opens an efficient pathway for nonradiative transition.<sup>7</sup> Spin-forbidden reactions are ubiquitous in transition metal compounds. Minimum energy crossing points (MECPs) in spin-forbidden reactions and minimum energy intersystem crossing (MEISC or ISC for short) points have attracted lots of scientific

concern because of their key roles in the reaction pathways.<sup>8–14</sup> Many research studies have revealed that these spin-changes can either accelerate the reactions or induce the reaction barriers.<sup>15–17</sup> The determinations of spin crossing geometries help to understand the reaction mechanism, explain the experimental phenomenon, and sometimes estimate the reaction rate.<sup>8,15,18,19</sup> In this article, the term MEISC point or ISC will be used in analogy to MECP, and we limit the discussion of MEISC (or ISC) only to the crossing of potential energy surfaces.

Methods for locating the MECPs can be classified into three as follows: the Lagrange multiplier method,<sup>9,20,21</sup> gradient projection method,<sup>22</sup> and penalty function method.<sup>23,24</sup> These methods have their own advantages and disadvantages.<sup>25</sup> Among the three, the penalty function method is very useful when derivative coupling vectors for the two-state intersection are unavailable,<sup>25,26</sup> for

example, when the computational model is large or the electronic structure method cannot calculate more than one electronic state simultaneously.<sup>7,27</sup> There are two typical penalty functions proposed by Ciminelli *et al.*<sup>23</sup> and Levine *et al.*,<sup>24</sup> respectively. Maeda *et al.* also used a simpler form of the Martinez type penalty function.<sup>28</sup> When locating MECP, one needs to prepare an initial structure that is better to be close to the real MECP, not only to save the computational resources but also to improve the degree of accuracy. Actual MECPs constitute a multidimensional seam on the potential surface. The optimized structure depends largely on the initial guess. For a spin crossing reaction, the situation is more problematic because several states with different spin multiplicities lie closely in energy. It is, therefore, not a straightforward task to prepare a proper starting point that leads to the MEISC point.

A significant number of computational methods have been developed to calculate TS. The most used methods can be divided into three groups based on the initial conditions. A class of methods such as the Newton–Raphson and quasi-Newton method starts from a proper guess of TS.<sup>29,30</sup> Methods such as the isopotential searching method start from the reactant.<sup>31</sup> The third class of methods begins with structures of the reactant and product. Among the third type, the nudged elastic band (NEB) method is one of the most widely used ones.<sup>32</sup> Since the original NEB method was developed, different variants were proposed to extend its applicable fields. Climbing image NEB (CI-NEB)<sup>33</sup> and improved tangent estimate NEB (IT-NEB)<sup>34</sup> were proposed in the same period. The former method made a small change to the image with highest energy. This climbing image does not feel the spring force but is optimized toward TS so that CI-NEB can yield TS while finding MEP without extra computational costs. IT-NEB highlighted a new way to estimate the local tangent to the path. A new tangent was said to be more stable and can help to eliminate the problem with kinks. There were also methods developed for improving the accuracy near TS by maintaining the proper density of images. Adaptive NEB (ANEb) and free-end NEB (FENEb) methods were proposed for this problem.<sup>35</sup> Recently, a combination of these two methods was published.<sup>36</sup> Another direction for the improvement is to accelerate the NEB calculation. Peterson introduced machine learning into the NEB method, while Koistinen and co-workers adopted the strategy to use Gaussian process regression.<sup>37,38</sup> All the improvements of the NEB method made until now were developed based on a single spin surface MEP searching.

As we have mentioned, the determination of the MEISC point bares another serious problem in addition to those of TS. Although our chemical intuition can give an initial guess to the TS structure, it is hard to do so for the MEISC point. Maeda and co-workers have a strategy to find all of the available crossing points by combining a penalty function method and automated search methods such as global reaction route mapping (known as GRRM) and the artificial force induced reaction (noted as AFIR).<sup>39</sup> On the other hand, we are interested in finding crossing points in the course of the reaction pathway. In this work, we will apply a penalty function method to the NEB method so that MEISC points can be automatically located while optimizing the reaction pathway. In Sec. II, a simple review about the traditional NEB method will be given. Then, the algorithm about the multiple spin-state NEB (MS-NEB) method will be discussed. The computational details about testing examples

will be stated in Sec. III. Section IV will show the results we tested.

## II. NUDGED ELASTIC BAND METHOD

### A. NEB method

The NEB method is a two-ending controlled method. By using optimized structures of the reactant ( $\vec{R}_0$ ) and product ( $\vec{R}_{N+1}$ ), a set of intermediate images  $\{\vec{R}_i | i \in [1, N]\}$  can be generated as the initial guess, where  $\vec{R}_i$  represents the Cartesian coordinate of image  $i$  and  $N$  represents the total number of intermediate images. Then, these images would be optimized iteratively under the influence of both the potential energy gradient and artificial spring force. This spring force is applied to avoid the images sliding into a minimum.

The linear interpolation (LI) method or the image dependent pair potential method is available for initial guess.<sup>40</sup> In this work, the LI method was adopted. The coordinate of image  $i$  is generated by

$$\vec{R}_i = \vec{R}_0 + \frac{i}{N+1} \cdot (\vec{R}_{N+1} - \vec{R}_0). \quad (1)$$

The objective function of the NEB method,  $S(\{\vec{R}_i\})$ , consists of the potential energy and spring energy,

$$S(\vec{R}_0, \dots, \vec{R}_{N+1}) = \sum_{i=1}^N V(\vec{R}_i) + \sum_{i=1}^{N+1} k_i/2 \times (\vec{R}_i - \vec{R}_{i-1})^2, \quad (2)$$

where  $k_i$  is a spring constant. The first term represents the summation of the potential energy, and the second term is the sum of the spring energy. To avoid the corner cutting problem or sliding problem,<sup>41</sup> only the perpendicular component (the component perpendicular to the reaction pathway, which is defined by the tangent) of the true force,  $\vec{F}_i^P|_{\perp}$ , and the parallel component of the spring force,  $\vec{F}_i^S|_{\parallel}$ , are adopted,

$$\vec{F}_i = \vec{F}_i^P|_{\perp} + \vec{F}_i^S|_{\parallel}, \quad (3)$$

$$\vec{F}_i^P = -\nabla V(\vec{R}_i), \quad (4)$$

$$\vec{F}_i^S = k_i [(\vec{R}_{i+1} - \vec{R}_i) - (\vec{R}_i - \vec{R}_{i-1})], \quad (5)$$

where  $\perp$  and  $\parallel$  mean perpendicular and parallel components, respectively. Superscripts  $P$  and  $S$  denote the potential force and spring force, respectively. See Fig. 1 for the direction of the vectors.

The climbing image (CI) NEB method<sup>33</sup> is a good choice if we want to locate TS at the same time. The image energetically on the top of the reaction pathway is optimized toward TS by using force

$$\vec{F}_{E_{max}} = -\nabla V(\vec{R}_{E_{max}}) + 2\nabla V(\vec{R}_{E_{max}})|_{\parallel}. \quad (6)$$

Considering the benefits of IT-NEB, we used this method as a good estimation of the tangent in this work. For more details of the tangent, the reader is referred to Ref. 34.

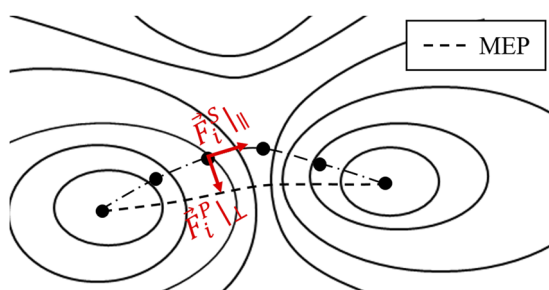


**FIG. 1.** Schematic illustration of the forces and the relation to MEP. Image  $i$  is driven to a point on the MEP under forces  $\vec{F}_i^{\perp}$  and  $\vec{F}_i^{\parallel}$  in Eq. (3). After all the images are converged together, they compose MEP.

## B. Multiple spin states NEB method

Our group has experiences of calculating the reaction systems related to ISC.<sup>42–47</sup> ISC points were found crucial to explain the experimental phenomena. Inspired by the CI-NEB method, the MS-NEB method is designed to locate the MEISC point with the framework of the normal NEB strategy. For simplicity, only two-state reactions will be discussed. This method, however, can be generalized for systems with more complicate multiple spin states, for example, three-state crossing at a certain structure by using an extended penalty function.<sup>7</sup>

The initial setting-up is the same as the normal NEB method. After the initial guesses are given, images will be optimized on the more stable spin surface. Spin multiplicity for each image is determined by comparing the single point energy of each spin state at a given coordinate.

Similar to the CI-NEB case, an image with the highest energy is appointed as CI for locating TS in the MS-NEB optimization, as shown in Eq. (6). If the spin multiplicity is changed between two images, one of the two can be optimized as the MEISC point. Hereafter, we call this selection scheme as two-image-selection. The objective function for the MEISC locating image is

$$S(\vec{R}_i) = (V_I(\vec{R}_i) + V_J(\vec{R}_i))/2 + \sigma \Delta V_{IJ}^2 / (\Delta V_{IJ} + \alpha), \quad (7)$$

where  $I$  or  $J$  refer to the higher and the lower energy states, respectively.  $\Delta V_{IJ}$  is energy difference between the two states and is defined as a positive number. The parameters  $\sigma$  and  $\alpha$  are constants, and their mathematical roles are discussed in the original paper.<sup>24</sup> In brief, the optimized structure converges to numerically exact the MEISC point if  $\sigma$  increases or  $\alpha$  approaches zero. Consequently, the force is derived as

$$\vec{F}_{ISC} = -(\nabla V_I + \nabla V_J)/2 + \sigma(\Delta V_{IJ}^2 + 2\alpha \Delta V_{IJ}) / (\Delta V_{IJ} + \alpha)^2 \cdot (\nabla V_I - \nabla V_J). \quad (8)$$

The major procedures of the MS-NEB method can be summarized in a flow chart, as shown in Fig. 2(a). In more details, the following steps were adopted:

1. Initial settings: input initial geometric information (the optimized structures of the reactant and product) and the

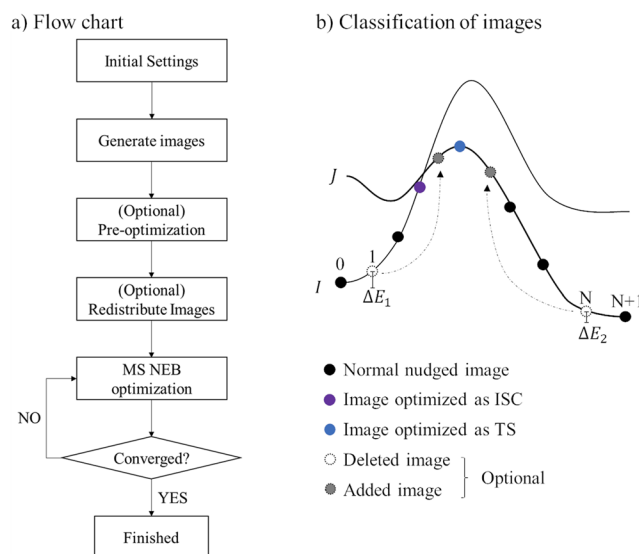


**FIG. 2.** (a) Flow chart of the algorithm of the MS-NEB method and (b) classification of images. States  $J$  and  $I$  have different spin multiplicity. The purple image will be optimized toward ISC, and the blue image will be optimized to TS, while the black images will be nudged. If the energy difference ( $\Delta E_1$ ) between images 1 and 0 is small enough, image 1 will be discarded and another image will be generated before TS. The same will be done to image  $N$ .

convergence criteria. In the following iterations, the displacement of each atom will be calculated by using mass-weighted Cartesian coordinates. Convergence of each image is declared if the total displacement becomes less than 0.0001 bohr, where the total displacement is the sum of the atomic displacements.

2. Image generations: generate coordinates of intermediate images by using the LI method. In the benchmark calculation below, 9–11 initial images were distributed as an ordinary NEB calculation. Although more images are often appreciated, more precision is compensated by more computation labor.
3. (Optional) Pre-optimization for several iterations (five iterations in this work): This step is designed for structural relaxation to avoid too bad initial geometries. Neither optimization to the MEISC point nor TS are performed in this step.
  - 3.1. First, carry out the SCF calculation for each spin state of each image.
  - 3.2. Determine the multiplicity of each image by comparing the energy of the two states. Use the force of the most stable spin state to optimize the images, where the force is given by Eq. (3).
  - 3.3. Exit if the convergence conditions (same criteria as mentioned in step 1) are met or the maximum number of iterations is reached. Or, go back to step 3–1.
4. (Optional) Redistribute images. If the energy difference of image 1 and the reactant is smaller than the certain

threshold (0.003 a.u. in this work), then image 1 will be discarded and a new image will be generated in between the image of the highest energy and its former image by taking the averaged coordinate [see Fig. 2(b)]. The same process is done between image N and the product. This step is intended to improve the image density around TS.

5. Main MS-NEB optimization iterations.
  - 5.1. SCF calculations are done as in step 3–1.
  - 5.2. The images are divided into three groups, as illustrated in Fig. 2(b). The one with the highest energy is optimized with the CI-NEB method by using the force of the most stable spin state. The MEISC point locating image is optimized with the force defined by Eq. (8). The rest are optimized by Eq. (3).
  - 5.3. Check the converged image numbers. If all the images are converged, the NEB optimization is normally finished. Otherwise, repeat step 5.

The computational labor of the MS NEB method should be mentioned in terms of the comparison with the ordinary single-state NEB method. To watch the relative energy order between two states, MS NEB performs two single-point calculations at one structure. For the climbing image toward the MEISC point, the objective function [Eq. (7)] also requires two single-point calculations. Therefore, the MS approach requires twice as much as the single-state NEB, assuming that the computational labor of two states is approximately equivalent.

The pre-optimization is intended to give more reasonable initial structures for the special images. Step 4 helps to avoid the waste of efforts on the area near the flat minima and increases the accuracy around TS. These two steps are, however, optional. In the main optimization step, an image for the MEISC point should be very carefully chosen as described later.

We note that the present NEB method is not designed for locating the energy minimum. The above-mentioned procedure is designed for the one-step reaction, which does not contain other minima except for the reactant and product states. If other minima were found on the reaction pathway, we suggest optimizing these minima separately. If these minima lie far from the reaction pathway, we also suggest performing MS-NEB calculations with adjacent minima pairs as the ending points.

In addition, with the purpose of improving the structure of the MEISC point, we proposed a stepwise MS-NEB method. Because of the spring force, the positions of the images have no negligible influence from the structure of TS. In the stepwise approach, a precise TS structure is located. Next, the reactant-TS and TS-product pairs of pathways were optimized with the MS-NEB calculation, as discussed in more detail in Subsection IV B.

For complex systems where spin crossing happens more than once, the near degeneracy of two states causes a serious difficulty in the two-image-selection scheme, which introduces too many crossing points. For the prescription, the three-image selection scheme was designed to avoid an artificially large number of special images during the pathway optimization. The schemes to determine the image optimized as the TS or MEISC structure will be explained in Sec. IV C. This three-image selection scheme requires no additional computation.

### III. COMPUTATIONAL DETAILS

We adopted the density functional theory (DFT) for all the calculations of potential energy. Exchange-correlation functionals and basis sets depend on the system. In the first example, C–C bond rotation of ethylene, the B3LYP functional with the 6-31G\* basis set was used for all the elements. In the second example, the C–H bond activation of methane by In<sub>2</sub>, the  $\omega$ B97XD functional, was adopted. The Stuttgart–Dresden basis set was used for indium, where 46 core electrons were replaced by the effective core potentials (ECPs) and the 6-31G\* sets for the others. The choice between a closed-shell and an open-shell calculation depends on molecule's spin state in two examples. The last example is a more complicated case where ISC happened twice in one reaction. Zhang and co-worker studied the methane activation by MH<sup>+</sup> (M = Fe, Co, and Ni) both experimentally and theoretically.<sup>48</sup> According to their result, all the three cases went through the ISC point twice. We tested CoH<sup>+</sup> as an example. To keep the consistency of the results, we adopted the same DFT functional and basis set as Zhang's work. In their study, an unrestricted B3LYP functional was used. As for the basis set, cc-pVTZ was applied for carbon and hydrogen. A Wachters (14s9p5d)/[8s4p3d] basis with two diffuse p functions, one diffuse d function, and a (3f)/[1f] polarization function was employed for cobalt. All the potential force was generated using the Gaussian 09 program package.<sup>49</sup> A quasi-Newton scheme, the Broyden–Fletcher–Goldfarb–Shannon (BFGS),<sup>50–54</sup> was implemented for the MS-NEB optimizer. The step size was evaluated by the line search method. According to the literature, the choice of spring constant is arbitrary because it only influences the image distribution along the path.<sup>41</sup> In the first and second examples, 0.1 was used for the spring constant. In the third example where the MEISC points are more than one, we adopted a larger value 0.5 for  $k_i$  to keep images reasonably spaced. We adopted 0.02 for  $\alpha$  [Eq. (7)] in all the examples. The  $\sigma$  value, which controls the energy gap, depends on cases as explained in each example.

### IV. BENCHMARK CALCULATIONS

#### A. MEISC point in C–C double bond rotation of ethylene

For the first and simplest example, the rotation of C–C double bond of ethylene was tested. Initially, the four hydrogen atoms are planar oriented as the equilibrium structure of ethylene. In this case, a closed-shell singlet state is the ground state. The C–C double bond is rotated until one CH<sub>2</sub> group becomes perpendicular to the other, and two 2p $\pi$  orbitals also become perpendicular in the final state, leading to the two 2p electrons being unpaired.

According to the intrinsic reaction coordinate (IRC) calculation, as the dihedral angle increases from 0° to 90°, the energy of the singlet state continuously grows up, while that of the triplet state decreases. In the present MS-NEB calculation, this tendency can be displayed in just one calculation, as shown in Fig. 3. Image 9 (I<sub>9</sub>) whose dihedral angle was 72.0° was automatically appointed to find the MEISC point. With the  $\sigma$  value of 3.5 [see Eq. (7)], the calculated energy gap of two spin states at convergence was 5.7 kcal/mol. The energy gap dropped to 4.1 kcal/mol when a larger  $\sigma$  value

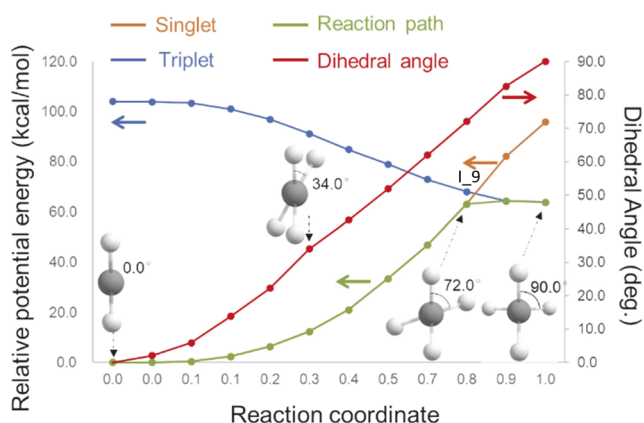


**FIG. 3.** Relative potential energy curves of ethylene C–C double bond rotation obtained by the MS-NEB method. Orange and blue lines are for singlet and triplet states, respectively. The green line represents the reaction pathway (singlet state from image 0 to image 10 and the triplet state from image 11 to image 12). The H–C–C–H dihedral angle of each image is represented by the red line. The definition of the reaction coordinate can be found in the [supplementary material](#).

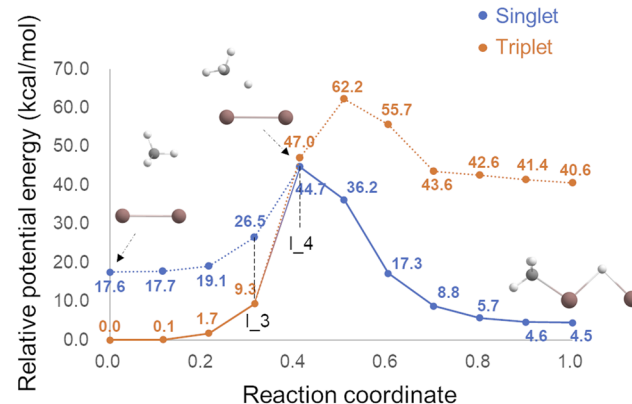
( $\sigma = 10$ ) was used without much structural change in the other images. When the  $\sigma$  value becomes even larger ( $\sigma = 30$ ), the degeneracy can be much improved within the gap of 0.1 kcal/mol. The dihedral values of the MEISC points calculated with  $\sigma = 3.5, 10,$  and  $30$  are  $72.0^\circ, 72.3^\circ,$  and  $72.3^\circ$ , respectively. The C–C bond lengths are 1.38 Å, 1.39 Å, and 1.45 Å, respectively. Obviously, the geometries optimized with larger a  $\sigma$  value are geometrically close to the refined MEISC point ( $\sigma = 30$ ). The relative energies of the three structures are 0.0 kcal/mol, 0.5 kcal/mol, and 2.5 kcal/mol, respectively, which also show the similarity.

## B. In-catalyzed C–H bond activation: A MEISC point proximal to TS

In our previous study, the intersystem crossing point was found in the C–H bond activation of methane catalyzed by  $\text{In}_2$ .<sup>55</sup> At the reactant side, methane and  $\text{In}_2$  were close to each other under intermolecular interaction. Because the ground state of  $\text{In}_2$  is the triplet state, the reactant state has triplet spin multiplicity. After  $\text{In}_2$  takes one hydrogen atom from the methane, homolytic dissociation of the C–H bond leads two unpaired electrons to couple with those of  $\text{In}_2$ . Thus, a singlet state is more favorable in the product state. Different spin states of the reactant and product states indicate the existence of the MEISC point.

The MS-NEB calculated reaction pathway with nine intermediate images is presented in Fig. 4(a). After the pre-optimization step, Image 4 (I\_4) was the highest point in the singlet state, and the triplet state was relatively higher than the singlet state. In this case, we put a higher priority on the TS optimization than the MEISC point optimization because TS is expected to be in MEP. Only image 4 was optimized as a transition state as CI-NEB, while other points were treated as normal nudged images. After the optimization, image 4 had the highest energy in the singlet state. At the same time, the spin-state change also happened between images 3 and 4. What is interesting in Fig. 4(a) is, although image 4 was only optimized as

(a) Intermediate image number equals to 9



(b) Intermediate image number equals to 10

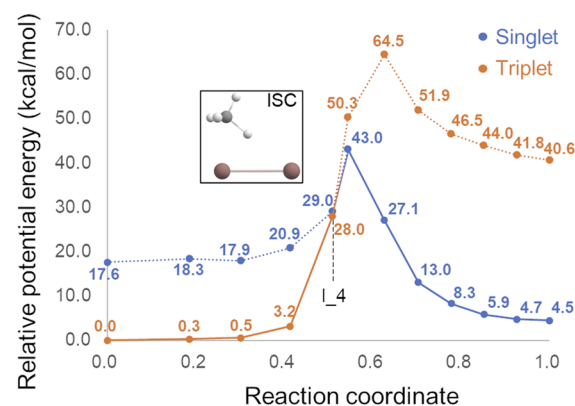


**FIG. 4.** (a) Relative potential energy profile of  $\text{In}_2$ -catalyzed C–H bond activation with nine intermediate images (No image was optimized as the MEISC point). (b) The relative potential energy profile of  $\text{In}_2$ -catalyzed C–H bond activation with ten intermediate images (one image was optimized as the MEISC point). The definition of the reaction coordinate can be found in the [supplementary material](#).

TS, the singlet-triplet energy gap is still smallest at this point, which is only 2.3 kcal/mol. In a word, image 4 was found to be the nearest point to both TS and ISC points. This means that the ISC can happen together with or at least near this TS. The structure information of important images can be found in Fig. S1 in the [supplementary material](#).

As discussed, there was no image optimized toward the MEISC point in the last calculation because of the proximity to the saddle point. In order to have a more precise MEISC point, we made a little change to the strategy of optimization. If one image meets the criterion of being both the TS and MEISC point, then it will be optimized as the TS while the neighbor will be optimized toward the MEISC point. Because the energy change from image 3 (I\_3) to image 4 (I\_4) is large in Fig. 4(a), we also increased the number of images to 10. The resulting energy profile is presented in Fig. 4(b), which keeps a similar tendency to Fig. 4(a). Besides, one MEISC structure, I\_4 in Fig. 4(b), was optimized with an acceptable

energy gap (1.0 kcal/mol). In this calculation, the  $\sigma$  value was set to 10.0. Because the degeneracy was already small enough, we did not refine the MEISC optimization with a larger  $\sigma$  value. The ISC point in Fig. 4(a) and the MEISC point in Fig. 4(b) were energetically different by about 17 kcal/mol. For the former calculation, we expected an MEISC point around 44 kcal/mol from the reactant state, as seen in Fig. 4(a), but it was located at only 28 kcal/mol in the later calculation. This result indicates the difficulty in setting up the initial guess of the MEISC point because the singlet and triplet energy surfaces are close to each other within a certain reaction coordinate range.

There is a possibility that the resultant MEISC point depends on the precision of the TS. When the CI-NEB calculation did not yield tightly converged TS due to limited image density,<sup>33,35,56</sup> an improvement in the TS structure could drag other images including the calculated MEISC point. Thus, if there is a demand for high precision of the MEISC structures, better TS geometries are required. Instead of optimizing TS and MEISC points simultaneously, the MS-NEB algorithm can be rearranged into sequential two steps, the TS optimization followed by the MEISC point optimization, which we, hereafter, call the stepwise MS-NEB method for clarity.

There are approaches to improve the accuracy of the TS structure. The ANEB method or two climbing image NEB (C2-NEB) methods can be combined with the MS-NEB method to find more accurate saddle points.<sup>35,57</sup> With a reliable TS, both reactant-TS and TS-product are two-ending pairs to run the MS-NEB calculations without climbing. Obviously, a larger computational resource is needed to achieve this algorithm. Because we focused on applying the NEB method in a spin-forbidden reaction, we simply used Gaussian09 to re-optimize the TS structure. With a fully optimized reactant, TS, and product, the reaction pathway was revised, as shown in Fig. 5. Image 5 (I<sub>5</sub>) was optimized as the MEISC point with a gap of 1.7 kcal/mol. Image 4 (I<sub>4</sub>) was dragged to approach the crossing region by the spring force; thus, the energy gap is as small as 1.9 kcal/mol. We note that, compared with Fig. 4(b), there is a small barrier in the singlet state before the transition state, as seen in

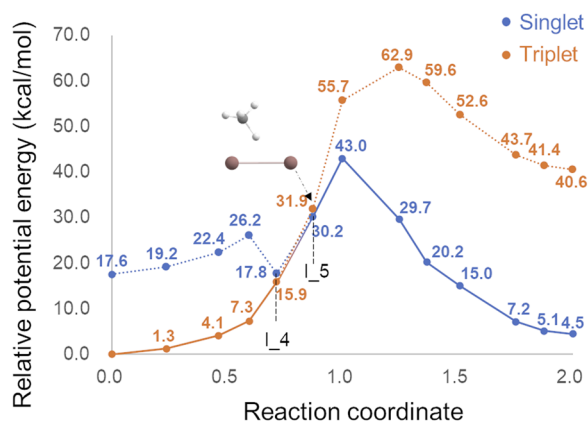
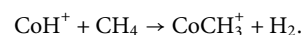


**FIG. 5.** The result of stepwise MS-NEB. Image 5 was optimized as the MEISC. The definition of the reaction coordinate can be found in the [supplementary material](#).

Fig. 5. This is because the images before the MEISC point were optimized on the triplet surface. In Fig. S5, the reaction pathways in two figures were represented by the points with different reaction coordinates. In this case, the MEISC points located by the stepwise MS-NEB (30.2 kcal/mol) and normal MS-NEB (28.0 kcal/mol) are energetically similar, indicating the effectiveness of normal MS-NEB. When the TS geometry predicted by the normal MS-NEB method is poor, stepwise MS-NEB is a better choice to optimize the MEISC points.

### C. Activation of methane by $\text{CoH}^+$ : Two-state reactivity

We also applied the MS-NEB method to a more complicated reaction,



According to DFT calculations by Zhang and co-worker,<sup>48</sup> a high spin state is the ground state at both reactant and product structures, while the low spin state is more stable near the TS region. Consequently, two MEISC points are expected in the reaction pathway.

For the cases where intersystem crossing may occur more than once along the reaction pathway, the images for optimization of the MEISC points should be chosen more carefully. For this example, a two-image-selection scheme was examined. An image would be optimized as an MEISC point if the neighboring image is the climbing image and has different spin multiplicity. An image is also treated as a MEISC point if two adjacent nudged images have different spin states and one has a smaller energy gap. However, this two-image-selection scheme failed in this example. The results calculated by using the two-image-selection scheme are shown in Fig. S3 in the [supplementary material](#). Because two surfaces lie closely, some minor structural changes transpose the energy order. As a result, several images were appointed as MEISC locating images, and unnecessarily many special points could be located. As described above, the special images do not feel the spring force and give a strange reaction pathway because they cannot be kept reasonably spaced.

To avoid generating unnecessary MEISC images, we proposed a three-image-selection scheme as shown in Fig. 6. Although a four-image-selection scheme would also be available, the three-image scheme can handle rather difficult problem such as two-state reactivity. In our premise, we assume that the distance between two images is small enough that the energy change is continuous and that the intersystem crossing happens only once in the sequential three images. Two cases would be recognized as candidates for MEISC points. In case 1 [Fig. 6(a), left], spin change happens between images  $i - 1$  and  $i$ , while spin states are the same for images  $i$  and  $i + 1$ . In addition, the energy gap at image  $i$  should be smaller than that of image  $i - 1$ . In Fig. 6(a), the right one is simply the mirror case of the left where the energy goes down. In case 2 [Fig. 6(b)], the left one as an example, spin states are different between images  $i$  and  $i + 1$  but keep the same between images  $i$  and  $i - 1$ . Besides, image  $i$  has a smaller energy gap than image  $i + 1$ . On the other hand, there is the case where image  $i$  is not optimized as an MEISC point. As shown in Fig. 6(c), the spin states of images  $i - 1$  and  $i + 1$  are the same but different from image  $i$ . It is assumed that

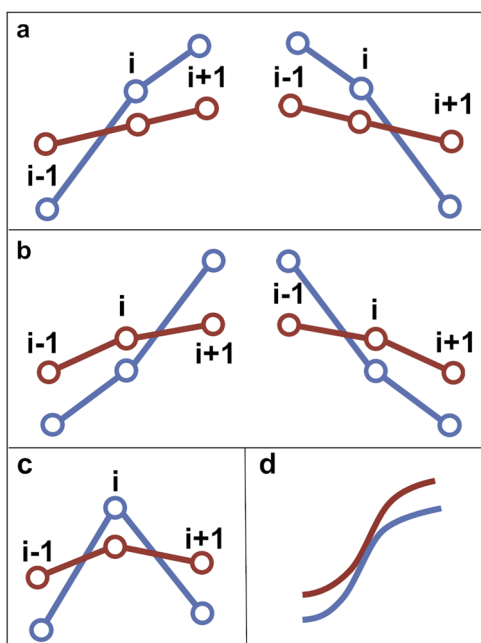


**FIG. 6.** Three-image-selection scheme for defining MEISC points. In the case of (a) and (b), image  $i$  will be recognized as the MEISC point. In the case of (c), image  $i$  will be nudged. Case (d) is an exceptional case and is excluded in the present study.

the step size is small enough that intersystem crossing is difficult to happen twice among the sequential three images. There could be a situation that two spin surfaces are crossing at a certain point, as shown in Fig. 6(d). However, this would be a very limited case and is out of our focus in the present study. On the other hand, because a one spin surface is always lower except for the crossing point, the spin crossing is less likely to happen. Thus, it is reasonable to omit such a crossing point. In the final calculation, this stricter scheme limited exactly two images to be MEISC points (image 3 and image 9 in Fig. 7).

The result of the three-image-selection scheme is shown in Fig. 7(a). Although the potential energy surfaces are basically similar to those obtained in the previous work,<sup>48</sup> we contributed the structures of the MEISC points in the present study. Image 4 ( $I_4$ ) was calculated as the transition state. Image 3 ( $I_3$ ) and image 9 ( $I_9$ ) were optimized as the MEISC point with 1.8 kcal/mol and 2.0 kcal/mol energy gaps, respectively. The first MEISC point was found just before the TS on the doublet surface. After the crossing, no extra energy is required to go over the TS. As shown in Fig. 7(b), the structure at  $I_3$  is very close to that of the TS on the doublet surface. On the other hand, the second MEISC point seems to be near the doublet minimum. Because the present version of the MS-NEB method does not locate the energy minimum, a separate optimization was performed at image 8 to confirm whether it is really close to the doublet minimum. From image 8, a slight  $H_2$  rotation and H-H shrink lead to the optimized structure, as shown in Fig. S4. The optimized minimum structure was more stable than image 8 by

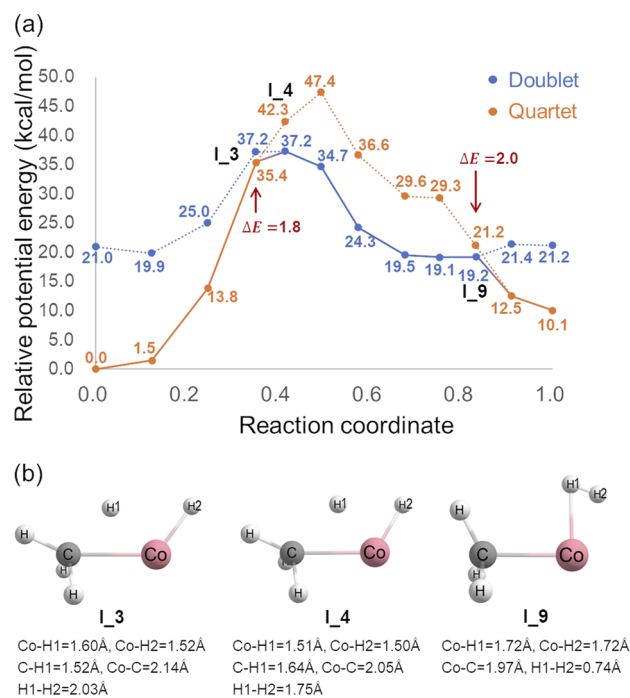


**FIG. 7.** (a) Reaction pathway of  $CoH^+$  catalyzed methane activation (two images,  $I_3$  and  $I_9$ , were optimized as MEISC points, and one image,  $I_4$ , was optimized as TS). (b) Geometric information of important images. The definition of reaction coordinate can be found in the [supplementary material](#).

only 2.3 kcal/mol, which confirmed that image 8 is not far from the doublet minimum. Thus, the transition from the doublet state to the quartet state should be very efficient. Because the minimum is close to the image obtained by the MS-NEB calculation, additional MS-NEB calculations by using the newly found minimum as the ending point was not performed. We also improved the  $\sigma$  parameter from 20.0 to 30.0 to perform a single ISC point optimization. An MEISC point structure was obtained near  $I_9$  whose energy difference was only 0.3 kcal/mol. As shown in Fig. 7(b), the H-H bond is already made at  $I_9$  and the electronic structure of  $[CoCH_3]^+$  relaxes to the stable quartet state.

## V. CONCLUSIONS

In this paper, we expanded the application scope of the NEB method to multi-spin systems. Here, we propose a new protocol, namely, the MS-NEB method, to solve the difficulty in defining an initial structure for the optimization of the MEISC point. The MS-NEB method can also automatically search out both the MEISC point and the saddle point while finding a reaction pathway that connects these critical points. This new method predicted reasonable results for the three benchmark calculations even in the complicated case where more than one MEISC point was located.

The MS-NEB method was tested for three systems: C-C rotation of ethylene, methane activation by  $In_2$ , and methane

activation by  $\text{CoH}^+$ . The second and the third examples suggest that the type of the image should be very carefully defined. For difficult cases where two surfaces with different spin stay close in energy, the optimized structures along the reaction pathway depend on which optimization scheme was used, as described in the  $\text{CoH}^+$  case. The choice of the two-image selection scheme or three-image scheme should depend on cases. According to our experience, if the intersystem crossing happens only once, the two-image-selection scheme performs well enough to handle the problem. If more than one MEISC point is expected, a relatively stricter standard three-image-selection scheme should be used. Besides, a reaction pathway with TS and the MEISC point can be obtained more precisely by optimizing TS and the MEISC point separately. In most cases, the normal MS-NEB is enough to evaluate the geometry of the MEISC point and TS. However, the use of the stepwise MS-NEB method is suggested for the precise optimization. Correspondingly, the stepwise MS-NEB method usually requires more computational cost. In the present study, we applied the MS-NEB method only to the two-state system. We note that it is possible to extend the method for more than two state systems by modifying the penalty function.

## SUPPLEMENTARY MATERIAL

See the [supplementary material](#) for important structural information, the result of the two-image-selection scheme for the  $\text{CoH}^+$  system, the simplified reaction coordinate for [Figs. 4\(b\)](#) and [5](#), the definition of the reaction coordinates, atomic coordinates of images, and original data in [Figs. 3–5](#) and [7](#).

## ACKNOWLEDGMENTS

This work was financially supported by JSPS KAKENHI (Grant Nos. JP15H05805 and 20H02685) and by MEXT (Integrated Research Consortium on Chemical Sciences). L.Z. thanks the China Scholarship Council (CSC) (Grant No. 201506340134) for their financial support. This research was also partly supported by the Photo-excitonix Project in Hokkaido University. Part of the computations was carried out at RCCS (Okazaki, Japan), ACCMS (Kyoto University), and RIIT (Kyushu University).

## DATA AVAILABILITY

The data that support the findings of this study are available within the article and its [supplementary material](#).

## REFERENCES

- M. A. Robb, F. Bernardi, and M. Olivucci, *Pure Appl. Chem.* **67**, 783 (1995).
- D. R. Yarkony, *Rev. Mod. Phys.* **68**, 985 (1996).
- D. R. Yarkony, *J. Phys. Chem.* **100**, 18612 (1996).
- D. R. Yarkony, *Acc. Chem. Res.* **31**, 511 (1998).
- D. R. Yarkony, *J. Phys. Chem. A* **105**, 6277 (2001).
- B. G. Levine and T. J. Martínez, *Annu. Rev. Phys. Chem.* **58**, 613 (2007).
- X.-Y. Liu, G. Cui, and W.-H. Fang, *Theor. Chem. Acc.* **136**, 8 (2016).
- J. N. Harvey, M. Aschi, H. Schwarz, and W. Koch, *Theor. Chem. Acc.* **99**, 95 (1998).
- N. Koga and K. Morokuma, *Chem. Phys. Lett.* **119**, 371 (1985).
- K. M. Smith, R. Poli, and J. N. Harvey, *New J. Chem.* **24**, 77 (2000).
- T. Chachiyo and J. H. Rodriguez, *J. Chem. Phys.* **123**, 094711 (2005).
- M. Lundberg and P. E. M. Siegbahn, *Chem. Phys. Lett.* **401**, 347 (2005).
- J. N. Harvey, *Phys. Chem. Chem. Phys.* **9**, 331 (2007).
- H. Hirao, D. Kumar, L. Que, and S. Shaik, *J. Am. Chem. Soc.* **128**, 8590 (2006).
- R. Poli and J. N. Harvey, *Chem. Soc. Rev.* **32**, 1 (2003).
- A. Fiedler, D. Schroeder, S. Shaik, and H. Schwarz, *J. Am. Chem. Soc.* **116**, 10734 (1994).
- D. Schröder, S. Shaik, and H. Schwarz, *Acc. Chem. Res.* **33**, 139 (2000).
- J. N. Harvey, R. Poli, and K. M. Smith, *Coord. Chem. Rev.* **238–239**, 347 (2003).
- J. N. Harvey, *Wiley Interdiscip. Rev.: Comput. Mol. Sci.* **4**, 1 (2014).
- D. R. Yarkony, *J. Phys. Chem.* **97**, 4407 (1993).
- M. R. Manaa and D. R. Yarkony, *J. Chem. Phys.* **99**, 5251 (1993).
- M. J. Bearpark, M. A. Robb, and H. Bernhard Schlegel, *Chem. Phys. Lett.* **223**, 269 (1994).
- C. Ciminelli, G. Granucci, and M. Persico, *Chem. Eur. J.* **10**, 2327 (2004).
- B. G. Levine, J. D. Coe, and T. J. Martínez, *J. Phys. Chem. B* **112**, 405 (2008).
- D. Sheppard, R. Terrell, and G. Henkelman, *J. Chem. Phys.* **128**, 134106 (2008).
- T. W. Keal, A. Koslowski, and W. Thiel, *Theor. Chem. Acc.* **118**, 837 (2007).
- G. Cui and W. Thiel, *J. Phys. Chem. Lett.* **5**, 2682 (2014).
- S. Maeda, K. Ohno, and K. Morokuma, *J. Phys. Chem. A* **113**, 1704 (2009).
- T. J. Ypma, *SIAM Rev.* **37**, 531 (1995).
- J. J. E. Dennis and J. J. Moré, *SIAM Rev.* **19**, 46 (1977).
- K. K. Irikura and R. D. Johnson, *J. Phys. Chem. A* **104**, 2191 (2000).
- G. Mills, H. Jónsson, and G. K. Schenter, *Surf. Sci.* **324**, 305 (1995).
- G. Henkelman, B. P. Uberuaga, and H. Jónsson, *J. Chem. Phys.* **113**, 9901 (2000).
- G. Henkelman and H. Jónsson, *J. Chem. Phys.* **113**, 9978 (2000).
- P. Maragakis, S. A. Andreev, Y. Brumer, D. R. Reichman, and E. Kaxiras, *J. Chem. Phys.* **117**, 4651 (2002).
- J. Zhang, H. Zhang, H. Ye, and Y. Zheng, *J. Chem. Phys.* **145**, 094104 (2016).
- A. A. Peterson, *J. Chem. Phys.* **145**, 074106 (2016).
- O.-P. Koistinen, F. B. Dagbjartsdóttir, V. Ásgeirsson, A. Vehtari, and H. Jónsson, *J. Chem. Phys.* **147**, 152720 (2017).
- S. Maeda, R. Saito, and K. Morokuma, *J. Phys. Chem. Lett.* **2**, 852 (2011).
- S. Smidstrup, A. Pedersen, K. Stokbro, and H. Jónsson, *J. Chem. Phys.* **140**, 214106 (2014).
- H. Jónsson, G. Mills, and K. W. Jacobsen, *Classical and Quantum Dynamics in Condensed Phase Simulations* (World Scientific, 1998), p. 385.
- F.-Q. Bai, N. Nakatani, A. Nakayama, and J.-y. Hasegawa, *J. Phys. Chem. A* **118**, 4184 (2014).
- S. Arulmozhiraja, N. Nakatani, A. Nakayama, and J.-y. Hasegawa, *Phys. Chem. Chem. Phys.* **17**, 23468 (2015).
- Y. Kitagawa, Y. Chen, N. Nakatani, A. Nakayama, and J.-y. Hasegawa, *Phys. Chem. Chem. Phys.* **18**, 18137 (2016).
- K.-j. Watanabe, N. Nakatani, A. Nakayama, M. Higashi, and J.-y. Hasegawa, *Inorg. Chem.* **55**, 8082 (2016).
- K. Oohora, H. Meichin, L. Zhao, M. W. Wolf, A. Nakayama, J.-y. Hasegawa, N. Lehnert, and T. Hayashi, *J. Am. Chem. Soc.* **139**, 17265 (2017).
- H. Nageh, L. Zhao, A. Nakayama, J.-y. Hasegawa, Y. Wang, and T. Nakano, *Chem. Commun.* **53**, 8431 (2017).
- Q. Zhang and M. T. Bowers, *J. Phys. Chem. A* **108**, 9755 (2004).
- M. J. Frisch, G. W. Trucks, H. B. Schlegel, G. E. Scuseria, M. A. Robb, J. R. Cheeseman, G. Scalmani, V. Barone, G. A. Petersson, H. Nakatsuji, X. Li, M. Caricato, A. Marenich, J. Bloino, B. G. Janesko, R. Gomperts, B. Mennucci, H. P. Hratchian, J. V. Ortiz, A. F. Izmaylov, J. L. Sonnenberg, D. Williams-Young, F. Ding, F. Lipparini, F. Egidi, J. Goings, B. Peng, A. Petrone, T. Henderson, D. Ranasinghe, V. G. Zakrzewski, J. Gao, N. Rega, G. Zheng, W. Liang, M. Hada, M. Ehara, K. Toyota, R. Fukuda, J. Hasegawa, M. Ishida, T. Nakajima, Y. Honda, O. Kitao, H. Nakai, T. Vreven, K. Throssell, J. A. Montgomery, Jr., J. E. Peralta, F. Ogliaro, M. Bearpark, J. J. Heyd, E. Brothers, K. N. Kudin, V. N. Staroverov, T. Keith, R. Kobayashi, J. Normand, K. Raghavachari, A. Rendell, J. C. Burant,

S. S. Iyengar, J. Tomasi, M. Cossi, J. M. Millam, M. Klene, C. Adamo, R. Cammi, J. W. Ochterski, R. L. Martin, K. Morokuma, O. Farkas, J. B. Foresman, and D. J. Fox, Gaussian 09 Rev. E.01, Gaussian, Inc., Wallingford, CT, 2016.

<sup>50</sup>C. G. Broyden, *IMA J. Appl. Math.* **6**, 76 (1970).

<sup>51</sup>R. Fletcher, *Comput. J.* **13**, 317 (1970).

<sup>52</sup>D. Goldfarb, *Math. Comput.* **24**, 23 (1970).

<sup>53</sup>D. F. Shanno, *Math. Comput.* **24**, 647 (1970).

<sup>54</sup>W. H. Press, S. A. Teukolsky, W. T. Vetterling, and B. P. Flannery, *Numerical Recipes in Fortran 77: The Art of Scientific Computing* (Press Syndicate of the University Cambridge, 1996).

<sup>55</sup>Y. Ohtsuka, Y. Nishikawa, H. Ogihara, I. Yamanaka, M. Ratanasak, A. Nakayama, and J.-y. Hasegawa, *J. Phys. Chem. A* **123**, 8907 (2019).

<sup>56</sup>S. A. Trygubenko and D. J. Wales, *J. Chem. Phys.* **120**, 2082 (2004).

<sup>57</sup>N. A. Zarkevich and D. D. Johnson, *J. Chem. Phys.* **142**, 024106 (2015).